1 SUPPLEMENTARY INFORMATION

1.1 Wrinkled Topography

We can find the conditions to have a well defined topography that is not modified by the presence of the patch. First, we reproduce the classical calculation to obtain the wrinkle wavelength of a bilayer and introduce the main parameters that we have used throughout the article. Assuming that the membrane is thin and has the highest stiffness of all the layers, we estimate its elastic energy when it is wrinkled with a wavelength λ as $U_B^{Memb} = (B_m/2)\int_S \kappa^2 dS \sim (B_m/2)(A/\lambda^2)^2 S$ where $S = bL$ and $B_m = E_m h^3/12(1-\nu_m^2)$. The substrate is thick and deforms by two ways: the compression of the whole substrate $U_0^{Subs} = (E_s/2)\int_V \epsilon^2 dV$ and the deformation of a layer of depth λ near the membrane that stores a strain $\epsilon_s \sim \partial_y u_x \sim A/\lambda$. It gives an energy for the substrate $U_S^{Subs} \sim U_0^{Subs} + (E_s/2)\epsilon_s^2 \lambda S$. Thus, the energy for the bilayer is

$$U_b \sim \frac{B_m}{2}\left(\frac{A}{\lambda^2}\right)^2 S + \frac{E_s}{2}\left(\frac{A}{\lambda}\right)^2 \lambda S + U_0^{Subs} \tag{1}$$

Because $A \approx \lambda\sqrt{\epsilon}$, energy minimization predicts a wavelength $\lambda \approx (B_m/E_s)^{1/3}$. It corresponds to the classical result that can be obtained with more precise theoretical methods [6, 7]. It is noteworthy that an important assumption of the presented derivation is a large mismatch between the stiffness of the membrane and substrate, or $E_m \gg E_s$.

When a thin patch, $\lambda \gg t$, is added to the bilayer, we need to add the energy of bending the patch. Assuming that the system has an unknown wavelength λ, we estimate the bending energy of the patch as $U_B^{Patch} = (B_p/2)\int_S \kappa^2 dS \sim (B_p/2)(A/\lambda^2)^2 S$ where $B_p = E_p t^3/12(1-\nu_p^2)$. Note that we are using the curvature of the membrane to describe the curvature of the middle surface of the patch. This is correct if $t\kappa, h\kappa \ll 1$ to neglect extra stretching energy because of rotation of the patch. The total energy of the three layer system (bilayer and patch) is

$$U_t = U_B^{Patch} + U_b \sim \frac{(B_m + B_p)}{2}\left(\frac{A}{\lambda^2}\right)^2 S + \frac{E_s}{2}\left(\frac{A}{\lambda}\right)^2 \lambda S + U_0^{Subs} \tag{2}$$

where we observe that for $B_m \gg B_p$ the bending energy of the patch can be neglected and then the wavelength is given by the interaction between the membrane and substrate. It includes the important case where the stiffness of the patch is larger than the stiffness of the membrane, $E_m \ll E_p$, but $h \gg t$ so that $B_m \gg B_p$.

In the thick patch limit, $\lambda \ll t$, the patch deforms in a similar way to the substrate: there is a compression of the whole patch and, because of the wrinkling, a layer of depth λ has an extra compressive strain $\epsilon_p \sim \epsilon_s \sim A/\lambda$. It gives $U_S^{Patch} \sim U_0^{Patch} + (E_p/2)\epsilon_p^2 \lambda S$. The total energy of the three layer is

$$U_t = U_S^{Patch} + U_b \sim \frac{B_m}{2}\left(\frac{A}{\lambda^2}\right)^2 S + \frac{(E_p + E_s)}{2}\left(\frac{A}{\lambda}\right)^2 \lambda S + U_0^{Subs} + U_0^{Patch} \tag{3}$$

Here we observe that the patch acts as a second substrate. We can neglect its effect in the determination of λ if $E_s \gg E_p$.

We conclude that the conditions given in Table 1 are sufficient to have a topography that is not the result of an elastic interaction between the patch and the membrane.

Table 1: Conditions to have a well defined topography for the bilayer

$\lambda \gg t$	$E_m \gg E_s$; $B_m \gg B_p$
$\lambda \ll t$	$E_m \gg E_s \gg E_p$

Finally, we observe that a sufficient condition to cover the thin and thick limits is $E_m \gg E_s \gtrsim E_p$. In the thick limit case, Eq. (3) implies that the wavelength can be estimated in general as $\lambda \approx [B_m/(E_s+E_p)]^{1/3}$. It shows that for $E_s \gtrsim E_p$ the patch could modify the original wavelength at most to the value $\lambda \approx 2^{-1/3}(B_m/E_s)^{1/3} \approx 0.8(B_m/E_s)^{1/3}$. In the thin limit, $\lambda \gg t$, or equivalently, $B_m \gg E_s t^3$, the condition $E_m \gg E_s \gtrsim E_p$ implies $B_m \gg E_s t^3 \gtrsim E_p t^3 \approx B_p$ which is the condition required in Table 1.

1.2 Silicone Patch Physical Experiment

An experimental set-up with controlled surface wrinkling was designed (see figure S1), to test topography induced surface de-adhesion in a model physical system mimicing the geometry of our simulations. The system is composed of two bilayers: a support bilayer and a wrinkling bilayer adhered under strain-mismatched conditions. The two bilayers are constructed using the same two polymers: S245 (Silicones, Inc., High Point, NC) as the softer component and RTV-4136M/Xiameter (Dow Corning, Midland, MI) as the stiffer component. Bulk samples of each fully cured silicone were tested using standard dog-bone tensile testing to obtain their respective Young's moduli: $E_s = 30$ kPa (S245) and $E_m = 3$ MPa (Xiameter). The support bilayer was constructed first by spreading a 1mm thick layer of RTV-4136M/Xiameter on an acrylic plate (McMaster-Carr, Elmhurst, IL) using 10:1 polymer:curing agent ratio from a solution of octane or hexane (percentage 10 weight percent) using a wire-wound rod with 0.0025 inch wire diameter and an automatic spreader (Paul N. Gardner Company, Pompano Beach, FL). After complete curing, a 250 μm S245 layer (10:2 ratio) was spread onto the 1mm Xiameter membrane; before allowing the second silicone to cure the support bilayer was placed into a custom built uni-axial stretch apparatus and stretched to a desired strain ϵ between $0 < \epsilon \lesssim 0.3$ (see figure S1). At this point, we placed onto the stretched support bilayer a wrinkling bilayer with the S245 substrate facing downwards (synthesis described below). The assembly now consisted of the support bilayer at 30 percent tensile strain, uncured S245 layer, and the wrinkling bilayer that was strain free by virtue of simply being laid down onto the stretched surface. The uncured S245 mid-layer was allowed to cure over 24 hours; after completion, the support and wrinkling bilayers

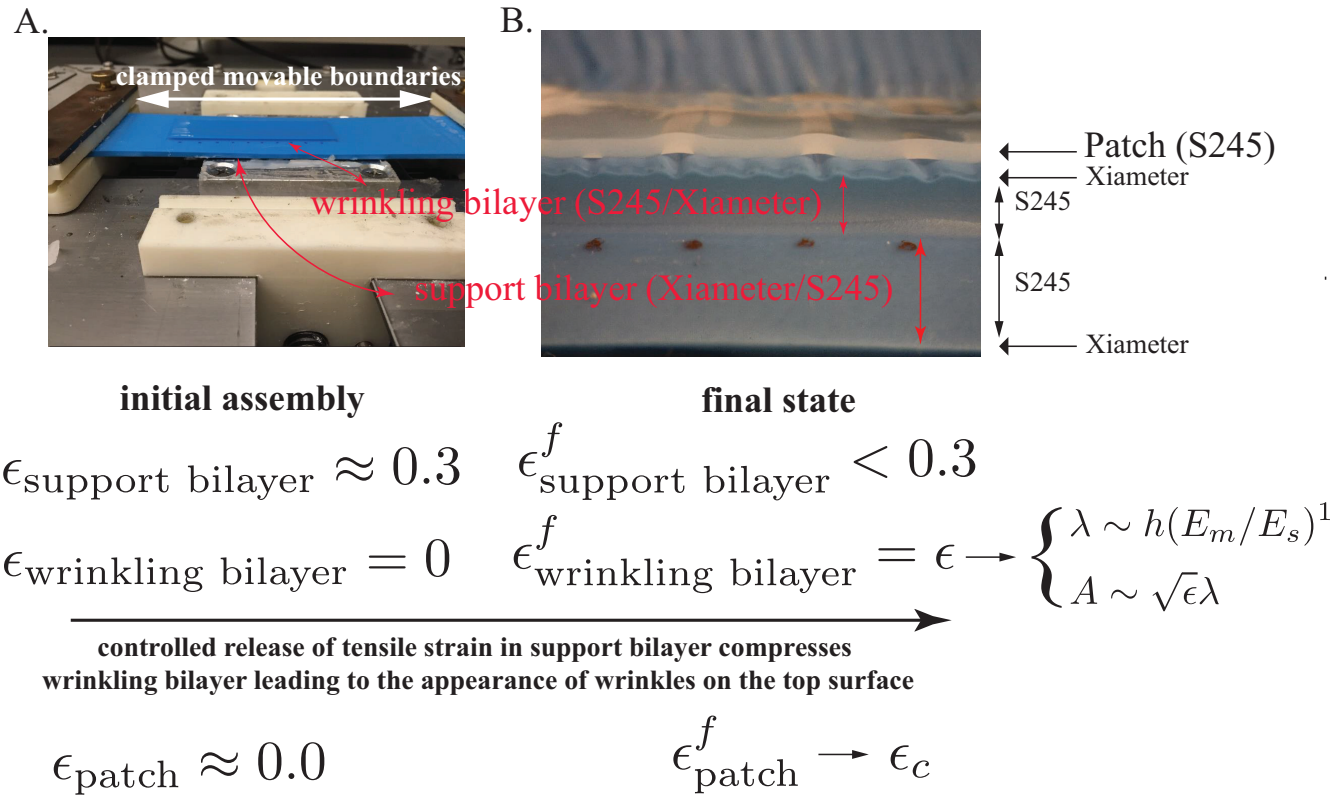

Fig. S 1: Picture of pre-stretch apparatus and bilayer assembly for experimental wrinkle induced patch de-adhesion experiments. The pictures shows the support bilayer, wrinkling bilayer, and patch. The initial assembly is such that the support and wrinkling bilayers are bonded in a strain mismatched configuration. As the strain is released in the support bilayer, wrinkles are generated on the top surface of the wrinkling bilayer. We follow the adhesion of the patch up to the point of de-adhesion. See supplementary videos 1 and 2 for representative data sets in thin and thick patch regimes.

were bonded in a strain mismatched configuration. By releasing the stretch (at approximate strain rates of 0.15 min^{-1}) on the support bilayer and given its larger thickness and stiffness, the wrinkling bilayer is compressed along its entire length generating wrinkles with wavelength $\lambda \sim h \times (E_m/E_s)^{1/3}$ and amplitude $A \sim \lambda\sqrt{\epsilon}$.

To obtain a wavelength in the $\lambda \sim 1500\,\mu$m range, a membrane thickness h on the order of a few microns was needed. The thin stiff membrane in the wrinkling bilayer was made by using 10:1 polymer:curing agent ratio of Xiameter in solution of octane or hexane (percentage ranged from 20 to 50 weight percent) and spreading a wet film using a wire-wound rod with 0.0025 inch wire diameter on-top of Acrylic plates. After the micron thin film fully cured, a 750 μm layer of S245 (10:1 polymer:curing agent ratio) was spread on-top and cured, generating the wrinkling bilayer that was used in the assembly described above and in generating the data for figure 5.

Having a controllable wrinkling surface with a precise measure of strain at each point, we turned to making S245 patches of varying thickness to function as the adlayers. Patches with thicknesses between 250 and 2750 μm were spread and cured. 1×3 cm rectangles were cut and placed onto the flat wrinkling bilayer surface (see figure S1). Once the tensile strain in the support bilayer was released and wrinkles developed in the wrinkling bilayer, the patch followed up to a critical point (ϵ_c) at which de-adhesion occurred (see figure 5, S1, and supplementary videos S1 and S2).

1.3 FEA Simulation Methods

Finite element simulations were performed using the commercial software package Abaqus v6.14 (Simulia, Dassault-Systemes, Providence, RI). To fully capture the highly non-linear aspects of the problem including the geometric non-linearity of surface buckling/wrinkling coupled with interfacial failure which introduces very complex contact problems, the simulations were carried out using the dynamic explicit solver in the mm-kg-ms system of units. The simulations were done using three-dimensional elements (C3D8R, 8-node linear brick, reduced integration, with hourglass control), however in order to optimize CPU time boundary conditions were used to create an effective plane-strain simulation, where the long wrinkle axis (proportional to the longitudinal axis in a wrinkling artery) was made much shorter than wrinkle wavelength.

The assembly consisted of three parts: substrate, membrane, and patch. Length ($x-$axis) and width ($y-$axis) were kept equal in all three parts. The thickness ($z-$axis) was adjusted proportionally. We first validated our wrinkling surface by assembling a bilayer composite with the thin membrane kinematically coupled to the substrate surface. By using the kinematic coupling constraint between the membrane bottom and substrate top surfaces in the $xy-$plane, we assure these surfaces behave as a perfectly bonded interface. The thickness of the substrate was chosen such that $H \geq 2\lambda$ for a given wavelength; this condition assured us that we would

be in the so called 'deep substrate limit' and that the well known wrinkle power law [4,5]

$$\lambda = 2\pi \left[\frac{(3-4\nu_s)(1-\nu_s^2)}{(1-\nu_s)^2}\right]^{1/3} \left(\frac{B_m}{E_s}\right)^{1/3} \tag{4}$$

should hold (as will be shown below) under plain strain conditions. Membrane thickness h, therefore, became our control parameter for setting λ. The material properties of the membrane and substrate were modeled as either linearly elastic or Neo-Hookean. For the linearly elastic case the Young's moduli were $E_m = 1.23$ GPa and $E_s = 0.01575$ GPa, which gave a modulus mismatch ratio of $E_m/E_s = 80$, and a Poisson ratio of 0.5. In the case of a Neo-Hookean material, the elastic strain energy is defined as

$$U_{NH} = C_{10}(\lambda_1^2 - 1) + D_1^{-1}(\lambda_1 - 2)^2 \tag{5}$$

where λ_1 is the first principal stretch ratio, $C_{10} = G/2$ (where G is the shear modulus), and $D_1 = 2/K$ (where K is the material bulk modulus). By using the virtual-work method, we obtain the non-linear stress-strain relation used in the simulation:

$$\sigma_{NH} = \frac{\partial U_{NH}}{\partial \lambda_1} = 2C_{10}\lambda_1 + 2D_1^{-1}(\lambda_1 - 2) \tag{6}$$

In dynamic explicit simulations, hyperelastic materials are more expensive from a CPU usage vantage than linearly elastic materials. In both cases, the computational efficiency of the simulation is dependent on the stable time increment that defines the minimum time between simulation steps: $\Delta t = L^e \cdot \left(\frac{E}{\rho}\right)^{-1/2}$, where L^e is the smallest mesh length, E is the largest modulus in the system, and ρ is the smallest density in the system. The simulation efficiency can be improved by using less stiff materials or coarser mesh. To optimize efficiency, the Neo-Hookean stiffnesses were chosen somewhat softer than in the linearly elastic case: for the membrane, $C_{10}^m = 0.00308$ GPa and D_1^m =16.238 GPa^{-1}, and for the substrate, $C_{10}^s = 2.843 \times 10^{-5}$ GPa and D_1^s =1301.07 GPa^{-1}. The ratio in moduli remained the same, $E_m/E_s = C_{10}^m/C_{10}^s = 80$. The above values of D_1 were selected to be equivalent to a Poisson ratio of 0.475 by using the standard relation $\nu = (3K/\mu - 2)/(6K/\mu + 2)$. By substituting $\nu = 0.475$ and $K/\mu = 1/(C_{10}D_1)$, the condition to select an appropriate D_1 becomes $1/(C_{10}D_1) = 20$. The choice of 0.475 was again made to optimize computational performance, since complete incompressibility within a dynamic explicit formulation leads to divergence in the stable time increment. The above material parameters for both the linear elastic and Neo-Hookean models are used to generate the wrinkling bilayer used in the simulations for patch deadhesion presented in figures 2 and 3. To generate wrinkles, the bilayer is compressed along its length ($x-$axis). Since the simulation is dynamic, the compression is defined as a velocity field applied to the the $yz-$planes at each end of the membrane and substrate. The initial displacement velocity was set to zero and smoothly increased over 0.5 ms to the target $v_x = 0.01$ mm/ms allowing for system equilibration. The

overall simulation time varied between $4 - 10$ ms. The choice of velocity and slow ramp was done to minimize kinetic energy in the system. Our goal is to use the broad versatility of the dynamic explicit solver to study a purely static elastic problem, mainly surface wrinkling and subsequently interfacial failure. To achieve this, the above boundary conditions and material properties were optimized to achieve a quasi-static solution early on in each simulation. Quasi-static solutions are those where the system kinetic energy is less than five percent of the total internal energy, which in the case of non-dissipative materials means that elastic strain energy comprises ninety-five percent of the total energy. During each simulation, kinetic, strain, and internal energies were continuously monitored to assure that the criterion for a quasi-static solution was always met. All other boundary conditions were applied such that overall the system could be considered meeting plane-strain conditions. To validate that the physics of surface wrinkling was correctly captured, a range of simulations was performed using different values of mismatch E_m/E_s and thickness h. Figure S2 shows the obtained wavelengths plotted against E_m/E_s and the corresponding scaling law given by the above defined power law for λ. Here we use $\nu_m = \nu_s = 0$ to simplify the simulations and avoid differences between plain stress and plane strain conditions, so that $\lambda = 2\pi(h/2^{2/3})\,(E_m/E_s)^{1/3}$. The good correspondence between the simulations and theory validates that our simulations capture surface wrinkling as expected for real elastic systems.

Having at our disposal a rigorously validated surface wrinkling model, whereby wrinkles appear naturally and evolve following the established scaling laws for elastic bilayers, we can turn to the problem of interest which is the stability of an attached adlayer/patch on a wrinkling surface. Element type and boundary conditions were equivalent to the above bilayers, the main differences include patch material property and the contact formulation between the patch bottom surface and membrane top surface. Mechanical properties of biologic materials are complex. In general, however, most biologic tissues are well modeled using hyperelasticity. To represent the behavior of a platelet patch, we use literature derived stress-strain data for a newly formed thrombus (S3) and model it using the generalized Ogden hyperelastic function. The data provided in reference (S3) have been successfully used in prior computational studies for arterial thrombus deformation (S4) and provide a well validated set for a biologically relevant foulant. Of note, the difference in global behavior of the Ogden and the simpler Neo-Hookean model, which can be reduced from the general Ogden form, is small; however, when performing experimental data fitting, the more generalized models give better approximations. A fourth-order Ogden functional is used:

$$U_{Ogden} = \sum_{i=1}^{4} \frac{2\mu_i}{\alpha_i^2}\left(\lambda_1^{\alpha_i} + \lambda_2^{\alpha_i} + \lambda_3^{\alpha_i} - 3\right) + \sum_{i=1}^{4} \frac{1}{D_i}\left(\lambda_1\lambda_2\lambda_3 - 1\right)^{2i} \tag{7}$$

where the best fit to the literature derived stress-strain data gives the coefficients in Table 2.

The energy functional is stable for a wide range of uniaxial and biaxial strains in the range -0.63 to 0.75. Approximations can be made for the initial elastic coefficients using $G_o =$

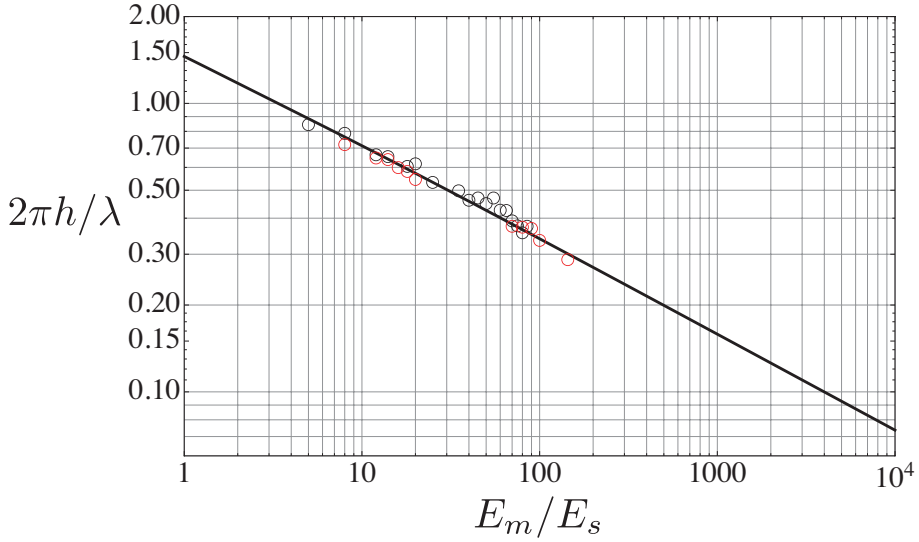

Fig. S 2: Plots $2\pi h/\lambda$ versus E_m/E_s for a range of mismatch values of our bilayer composite (circles). The solid black line is given by the scaling law $\lambda = 2\pi(h/2^{2/3})\,(E_m/E_s)^{1/3}$ valid for $\nu_s = \nu_m = 0$. The excellent fit validates that our bilayer simulation captures the expected wrinkling physics correctly.

Table 2: Ogden coefficients

i	μ_i	α_i	D_i
1	1.7147×10^{-6}	1.9997	270703.3690
2	5.4766×10^{-7}	4.0000	0
3	-6.9116×10^{-7}	-2.0000	0
4	1.1942×10^{-8}	-4.0000	0

$\sum_{i=1}^{4} \mu_i \approx 1.583 \times 10^{-6}$ GPa or 1500 Pa, which is in the appropriate range of magnitude for a very soft biologic material. Likewise, $K_o = 2/D_1 = 7.388 \times 10^{-6}$ GPa, which using the above relation gives an effective Poisson ratio of 0.4.

Interfacial failure requires careful model considerations as it introduces a great deal of non-linearity into the numerical solutions; most importantly, after failure, new surfaces are created leading to discontinuities across boundaries that were once continuously differentiable. Working within the general contact formulation of the dynamic explicit solver, we modeled the patch/membrane interface using a cohesive zone model (CZM) (S5, S6, S7). We defined a mode-independent traction-separation law: $\sigma_{coh} = k_c \delta_{coh}$, where the interfacial stress σ_{coh} is linearly related to the separation distance between patch bottom and membrane top surfaces δ_{coh}, with the cohesive stiffness set by $k_c = 0.2$ kN/mm^3 (S5). Stress develops within the interface following the traction-separation law as the surfaces deform with the global deformation up to a point, where interfacial failure occurs and a crack propagates. The failure stress is defined by inputing the maximum interfacial separation parameter $\delta_{coh} = \delta_{max}$. In our model, once the failure criterion is met the interfaces are free to separate and we do not model any post-failure interfacial softening. This allows a simple connection to interfacial thermodynamics via the scaling relation $\gamma \sim \sigma_{coh}\delta_{coh} = k_c \delta_{coh}^2$ (S5). In our model, we keep k_c constant and vary $\delta_{max} = \delta_{coh}$ at which interfacial failure occurs to study various adhesion strengths. Even though the relationship between adhesion strength and fracture energy is complex, the method of cohesive volumetric finite element modeling using traction separation laws has been well validated in multiple technical studies (S5, S6).

The critical point at which de-adhesion occurs is defined by tracking the contact area between patch bottom and membrane top surfaces ($A_{contact}$). By definition, $A_{contact}$ is constant until interfacial failure between the membrane and patch initiates and decays to zero ($A_{contact} \to 0$) when the entire interface has failed. We define the critical point and therefore $A_c(\kappa_c)$ as the point when $A_{contact}$ has decreased by 5% from its initial constant value (see figure S3). This quantitative definition correlates very closely to a more qualitative measure obtained by visually inspecting the simulation output graphics and defining A_c at the point where A_ℓ becomes first noticeable. Of note, as shown in figure S3, there is a region of stable delamination that does not correspond to any global shape change (see supplementary videos 3, 4, and 5) prior to A_c. This stable delamination is predicted in the main text and figure 4.

1.4 Elastic Energy Color Map

In figure 2 of the text we do not provide the color map explicitly. Figure S4 provides this in terms of kN-mm, given that the simulations are performed in mm-kg-ms consistent units.

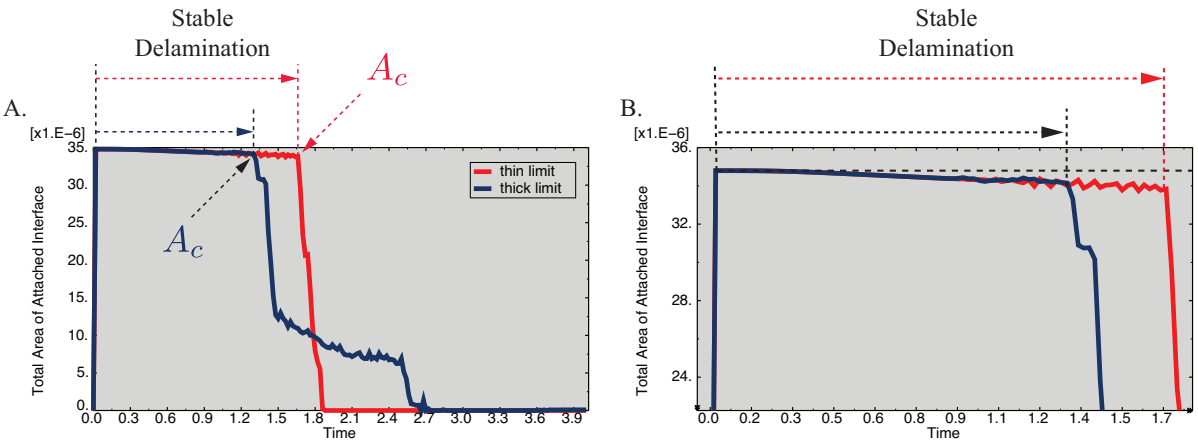

Fig. S 3: A. Total area of attached interface between top membrane surface and bottom patch surface for representative thin and thick patch simulations (see supplementary videos 3, 4, and 5). The time at A_c correlates well to appearance of macroscopic delamination in the simulation videos, this corresponds to the defined theoretical critical point in the main text. Once A_c is reached the interfacial crack becomes unstable and propagates spontaneously. B. Zoom view of A. It is noteworthy, that even prior to A_c, there is a slow and small decrease in attached area. This stable microscopic delamination does not lead to any appreciable global shape changes (see supplementary videos 3, 4, and 5), and likely corresponds to crack regions whose length is the order of a single finite element.

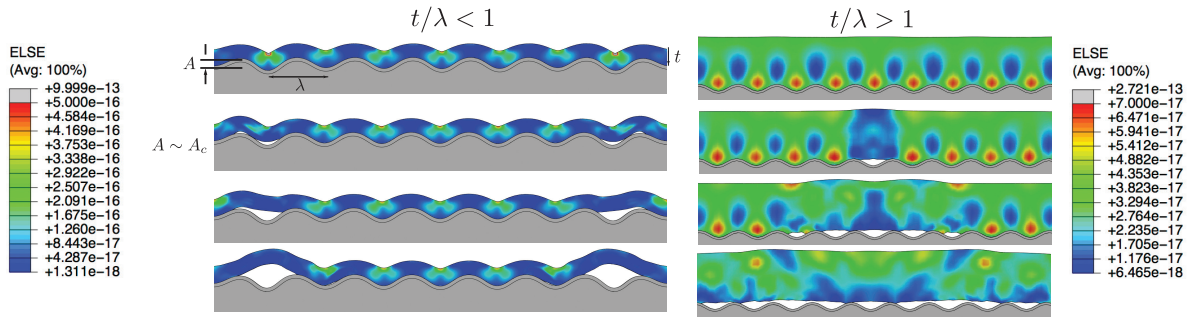

Fig. S 4: Thin and thick regime simulations as shown in figure 2 (main text), with the elastic strain energy scales shown in kN-mm.

1.5 Thin and Thick Limit Crossover Analysis

To check the scaling relation $B_p A_c/\lambda^2 = c \times \gamma^{1/2}$ for the thin limit, we first study the numerical data corresponding to $t/\lambda < 0.2$, a very cautious definition for the data in the thin limit case. It gives the best fit for a dimensionless prefactor $c \approx 0.134$. In a second stage, we fix c to the value obtained from the previous analysis and use the relation

$$B_d A_c/\lambda^2 = c \times \gamma^{1/2} \tag{8}$$

where $B_d = E_p d^3/12(1-\nu_p^2)$ and d is the penetration length defined as

$$d = \begin{cases} t & t < \lambda/p \\ \lambda/p & t > \lambda/p \end{cases}$$

Using all the data collected for N different numerical experiments, we obtain the difference $E = \sum_{i=1}^{N} [\ln(B_d A_c/\lambda^2)_i - \ln(c \times \gamma^{1/2})_i]^2$ as a function of the free parameter p. The function $E = E(p)$ has a minimum for $p \approx 2.4$ that minimizes the error in the log-log fit of figure 3.

1.6 Supplementary Videos

Five supplementary videos are provided to help show the mechanism in real time. Representative videos are chosen for both the thin (supplementary videos 1 and 3) and thick (supplementary videos 2, 4, and 5) patch regimes. Videos 1 and 2 are of the experiments and videos 3, 4, and 5 are from the simulations. In the thin patch regime, the patches follow the topography coming from the wrinkling surface up to a critical point where they delaminate into less curved blisters several times the length of the wavelength ($\ell > \lambda$). In case of the thick patch regime, the patch is deformed locally nearly the wrinkling interface but does not globally bend, once delamination occurs the patch remains globally flat. The videos show the strong visual similarity in the initial and final shapes of the patch pre and post-interfacial failure between the experimental and numerical systems in both thin and thick regimes.

1.7 Data Availability Statement

The data that support the plots within this paper and other findings of this study are available from the corresponding author upon request.

References

S1. Yang, S., K. Khare, and P.-C. Lin, *Harnessing surface wrinkle patterns in soft matter.* Advanced Functional Materials, 2010. **20**: p. 2550.

S2. Ye, S.H., et al., *Hollow Fiber Membrane Modification with Functional Zwitterionic Macromolecules for Improved Thromboresistance in Artificial Lungs.* Langmuir, 2015. **31**: p. 2463-2471.

S3. Xie, H., Kim, K., Aglyamov, S.R., Emelianov, S.Y., O'Donnell, M., Weitzel, W.F., Wrobleski, S.K., Myeres, D.D., Wakefield, T.W., and J.M. Rubin. *Correspondence of Ultrasound Elasticity Imaging to Direct Mechanical MEasurement in Aging DVT in Rats.* Ultrasound in Medicine and Bioogy., 2005. **31**: p. 1351-1359.

S4. Vahidi, B., and N. Fatouraee. *Large deforming buoyant embolus passing through a stenotic common carotid artery: a computational simulation..* Journal of Biomechanics, 2012. **45**: p. 1312-1322.

S5. Dantuluri, V., Maiti, S., Geubelle, P.H., Patel, R., and Hakan Kilic. *Cohesive modeling of delmainatino in Z-pin reinforced composite laminates.* Composites Science and Technology, 2007. **67**: p. 616-631.

S6. Turon A., Camanho, P, and Costa J. *Delamination in Composites: Simulation of Delamination in Composites under Static and Fatigue Loading Using Cohesive Zone Models* VDM Verlag Dr. Muller, Berlin, Germany, (2008).

S7. Barbero, E.J. *Finite Element Analysis of Composite Materials with ABAQUS* Ch 10 - Delaminations, CRC Press, Boca Raton, FL, (2013), pp. 356-371.

S8. Greensmith, E. and B.R. Duling. *Morphology of the Constricted Arterioloar Wall - Physiological Implications.* American Journal of Physiology, 1984: **247**: H687-H698.